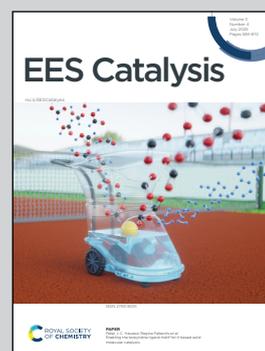**Showcasing research from Prof. Chang Won Yoon's lab., Pohang University of Science and Technology, Republic of Korea.**

Direct electrolysis of liquid anhydrous ammonia for continuous production of high-purity, pressurized hydrogen at ambient temperature

$NH_3$ is valued as a large-scale $H_2$ carrier due to its high $H_2$ storage capacities (≥108 kg-$H_2$ m$^{-3}$, 17.7 wt%) and simple liquefaction conditions (25 °C at 10 bar). However, producing high-purity and pressurized $H_2$ *via* catalytic $NH_3$(g) thermolysis requires high temperatures (>600 °C) with multiple purification and compression steps. Here, we present a proof-of-concept study using a zero-gap liquid anhydrous $NH_3$ electrolyzer comprising electrocatalysts and a cation exchange membrane that directly converts gap liquid anhydrous $NH_3$ into high-purity (>99.99%) and pressurized (>5.5 bar) $H_2$ at 10 °C with a Faradaic efficiency of >98.8%.

Image reproduced by permission of Chang Won Yoon from *EES Catal.*, 2025, **3**, 694.

**ROYAL SOCIETY OF CHEMISTRY**

rsc.li/EESCatalysis

# EES Catalysis

Check for updates

# Direct electrolysis of liquid anhydrous ammonia for continuous production of high-purity, pressurized hydrogen at ambient temperature†

Seungmok Han, [ID] [ab] Junsoo Ha,[a] Jae Seung Lee,[a] Hyukjoo Lee,[c] Chang Hyun Lee,[c] Kangwoo Cho [ID] [b] and Chang Won Yoon [ID] ★[a]

The direct electrolysis of liquid anhydrous ammonia ($NH_3(l)$, >99.99% of $NH_3$, free of water and solvent) is demonstrated using a 25 cm² zero-gap electrolyzer, consisting of a Ru/C anode and a Pt/C cathode, with the two electrodes spatially separated by a cation exchange membrane. This system, supplied by $NH_3(l)$ and $NH_4Br$ as the supporting electrolyte, continuously produces high-purity and pressurized hydrogen ($H_2$, >99.99%, >5.5 bar) at a temperature of 10 °C and a pressure of 6.2 bar, without requiring $H_2/N_2$ separation and compression processes. The direct $NH_3(l)$ electrolyzer exhibits a cell potential of 1.1 V at 0.1 A cm⁻², presenting a faradaic efficiency of >99.3% for $H_2$ production. The developed system achieves a $H_2$ production rate of >18.8 mol-$H_2$ $g_{cat}^{-1}$ h⁻¹ at 0.5 A cm⁻², which is 4.7-fold higher than the highest $H_2$ production rate reported to date for $NH_3(g)$ thermolysis at temperatures of over 500 °C.
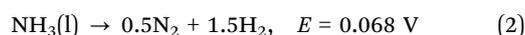
## Introduction

Hydrogen ($H_2$) is a promising renewable energy carrier owing to its high gravimetric energy density (33.3 kWh kg-$H_2^{-1}$) and environmentally benign properties. However, its low volumetric energy density (3 kWh m⁻³ at 20 °C, 1 bar) poses a substantial scientific challenge, particularly for its large-scale storage and long-distance transportation.[1–3] To address these limitations, green and/or blue ammonia ($NH_3$) has been proposed as a promising $H_2$ carrier due to its high volumetric $H_2$ storage capacity ($\geq$108 kg-$H_2$ m⁻³),[4–7] and ease of liquefaction (*e.g.*, 25 °C, 10 bar). The transported liquid anhydrous $NH_3$ ($NH_3(l)$, >99.99% of $NH_3$, free of water and

[a] *Department of Chemical Engineering, Pohang University of Science and Technology (POSTECH), Pohang, 37673, Republic of Korea.*
*E-mail: cwyoon@postech.ac.kr*

[b] *Division of Environmental Science and Engineering, Pohang University of Science and Technology (POSTECH), Pohang, 37673, Republic of Korea*

[c] *Department of Energy Engineering, Dankook University, Cheonan, 31116, Republic of Korea*

† Electronic supplementary information (ESI) available: Document S1: equations of ammonia electro-oxidation reaction S1–S3, Notes S1–S4, Fig. S1–S12, Tables S1–S3 and references. See DOI: https://doi.org/10.1039/d5ey00140d
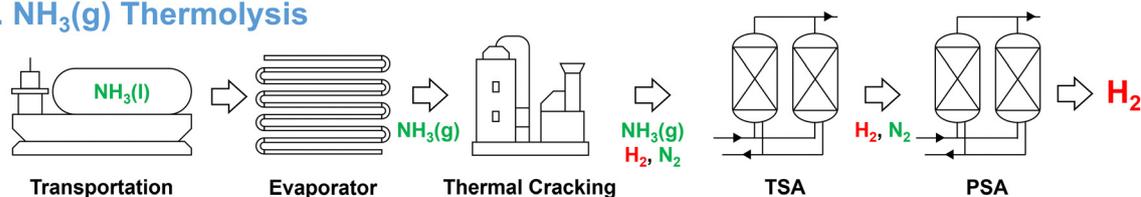
### Broader context

Hydrogen ($H_2$) is a key energy carrier that resolves the imbalance between renewable energy production and demand, contributing to global carbon neutrality. However, the low volumetric energy density of gaseous $H_2$ (3 kWh m⁻³ at 20 °C, 1 bar) poses challenges for large-scale storage and transportation. To address this limitation, ammonia ($NH_3$) has gained significant attention as a sustainable $H_2$ carrier due to its superior $H_2$ storage capacity and simple liquefaction conditions (10 bar at 25 °C). $NH_3(g)$ thermolysis for hydrogen production is currently being developed for commercial implementation, but it requires high reaction temperatures (>600 °C) with multi-step purification, separation and compression processes. This study presents a proof-of-concept demonstration of the direct electrolysis of liquid anhydrous $NH_3$ (>99.99%, water/solvent-free) to produce $H_2$ at near-ambient temperature (10 °C). The zero-gap $NH_3(l)$ electrolyzer, designed with electrocatalysts and a cation exchange membrane, enables the production of high-purity (>99.99%) and pressurized (>5.5 bar) $H_2$ in a single process. Our developed system achieves a faradaic efficiency of >98.8% and a 4.7-fold higher $H_2$ production rate compared to the state-of-the-art $NH_3(g)$ thermolysis. The proposed continuous $NH_3(l)$ electrolyzer offers an alternative $H_2$ production model from $NH_3$, potentially improving the cost efficiency and flexibility of $H_2$ generation facilities.

solvent) can then release $H_2$ on demand through thermal cracking, releasing only nitrogen ($N_2$) as a byproduct, as shown in eqn (1). However, due to its endothermic nature, most of the processes currently being developed to thermally crack $NH_3(g)$ typically require high temperatures exceeding 600 °C and even higher temperatures are needed to obtain high-pressure $H_2$.[8] Accordingly, a thermally enhanced $NH_3(g)$ dehydrogenation process integrated with multistep separation procedures may be suitable for a centralized $H_2$ production facility (Fig. 1A).[9,10]

$$NH_3 \rightarrow 0.5N_2 + 1.5H_2, \quad \Delta H = +46 \text{ kJ mol}^{-1} \quad (1)$$

$$NH_3(l) \rightarrow 0.5N_2 + 1.5H_2, \quad E = 0.068 \text{ V} \quad (2)$$

As an alternative strategy, electrochemically converting $NH_3$ to $H_2$ has been proposed. Two concepts for the electrolysis of $NH_3$ exist: (i) aqueous $NH_3$ electro-oxidation reaction (AOR, $NH_3(aq)$, Fig. 1B)[11–13] and (ii) direct electrolysis of liquid
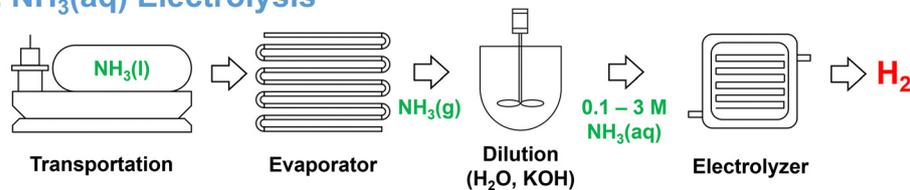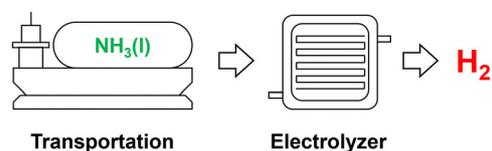
## A. NH$_3$(g) Thermolysis



## B. NH$_3$(aq) Electrolysis



## C. NH$_3$(l) Electrolysis



Fig. 1    Schematic illustration of three H$_2$ production methods utilizing NH$_3$. (A) Thermolysis of NH$_3$(g). (B) Ammonia electro-oxidation reaction (AOR) of diluted NH$_3$(aq). (C) Direct electrolysis of NH$_3$(l).
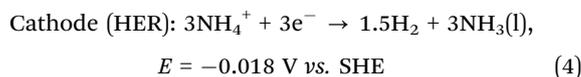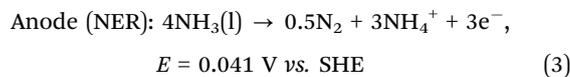
anhydrous NH$_3$ (NH$_3$(l), Fig. 1C).[14–17] Compared with the potential of water electrolysis (+1.23 V),[18,19] these methods lower the cell voltage ($E_{cell}$) to 0.060 V for the AOR (eqn (S1)–(S3), ESI†) and 0.068 V for direct NH$_3$(l) electrolysis (eqn (2) and Note S1, ESI†), thereby potentially achieving high energy efficiency for H$_2$ production. For the AOR, however, diluted aqueous NH$_3$(aq) solutions (*ca.* 0.1–3 M, 0.2–5 wt%) with potassium hydroxide (KOH, *ca.* 0.1–7 M, 0.6–30 wt%) in distilled H$_2$O are commonly used,[20–22] which require additional chemicals and waste treatment facilities, thus potentially increasing the cost of H$_2$ production. In addition, anodic N$_2$ production in the AOR competes with the oxygen evolution reaction in water electrolysis, possibly leading to the formation of byproducts such as NO$_x$.[23,24] Thus, cell operation at a high current density is limited, making it challenging to achieve a high H$_2$ production rate.

In contrast, direct NH$_3$(l) electrolysis requires no water addition and can be conducted under ambient temperature. In addition, NH$_3$(l) has favorable liquefaction conditions (25 °C at 10 bar) and appropriate viscosity (1.57 mPa s at 20 °C) for electrolysis.[25] Moreover, the volumetric and gravimetric H$_2$ storage capacities of NH$_3$(l) are higher than those of H$_2$O (112 kg-H$_2$ m$^{-3}$ and 11.2 wt%). Previously, pioneering studies on NH$_3$(l) electrolysis using metal plates or disks in a batch reactor by adding either anionic (KNH$_2$, NaNH$_2$) or cationic (NH$_4$PF$_6$) supporting electrolyte have been shown to achieve H$_2$ generation.[14–16] However, the basic electrochemical properties (*e.g.*, anode/cathode potentials, overpotential and Tafel slopes) of the active metals used for NH$_3$(l) electrolysis have not been elucidated. Moreover, separation processes for the produced H$_2$/N$_2$ mixed gases are still necessary to obtain high-purity H$_2$ due to the limitations of batch reactions on small scales. Therefore, designing an efficient and scalable electrolysis system that enables the continuous production of high-purity H$_2$ in a flow reactor and acquiring fundamental parameters associated with NH$_3$(l) electrochemical reactions is necessary.

Here, we describe a continuous system for the direct electrolysis of NH$_3$(l) to produce high-purity and pressurized H$_2$. Potential anode and cathode active metals are initially screened in a batch reactor. Subsequently, a zero-gap type electrolysis cell, configured with a Ru/C anode and Pt/C cathode, each with an active area of 25 cm$^2$ on carbon foam and NH$_4$Br as a supporting electrolyte, is designed and operated under near-ambient temperature and pressurized conditions (10 °C, 6.2 bar). The developed electrochemical splitting system utilizing NH$_3$(l) demonstrates the continuous production of high-purity and pressurized H$_2$ (>99.99%, >5.5 bar) without a H$_2$/N$_2$ separation process, achieving a faradaic efficiency of >98.8% for H$_2$ production.

## Results and discussion

$$\text{Anode (NER): } 4NH_3(l) \rightarrow 0.5N_2 + 3NH_4^+ + 3e^-,$$
$$E = 0.041 \text{ V } vs. \text{ SHE} \tag{3}$$

$$\text{Cathode (HER): } 3NH_4^+ + 3e^- \rightarrow 1.5H_2 + 3NH_3(l),$$
$$E = -0.018 \text{ V } vs. \text{ SHE} \tag{4}$$

$$K_{eq} \text{ of } 2NH_3(l) \leftrightarrow [NH_4^+][NH_2^-] = 10^{-33} \text{ (223 K)} \tag{5}$$

Because most of the electrochemical reactions studied to date are defined in aqueous media, calculating the theoretical potentials of the N$_2$ (nitrogen evolution reaction: NER) and H$_2$ (hydrogen evolution reaction: HER) evolution reactions for the direct electrolysis of NH$_3$(l) is necessary. When the partial

pressures of $H_2$ and $N_2$ are considered, the theoretical potentials for the NER and HER in the batch system are calculated as 0.041 and $-0.018$ V (eqn (3), (4) and Note S1–S3, ESI†), respectively, yielding an overall cell potential of 0.059 V. To screen potential catalysts for the electrolysis of $NH_3(l)$, we initially design a semi-batch reactor using $NH_4Br$ (1 M) as a supporting electrolyte (Fig. S1, ESI†) in $NH_3(l)$ media. In this system, ammonium ions ($NH_4^+$) serves as a charge carrier and acts as a conjugated acid due to the autoionization property of $NH_3(l)$ into $NH_4^+$ and amide ions ($NH_2^-$) (eqn (5)), similar to water ($2H_2O \rightarrow H_3O^+ + OH^-$). Standard electrodes are fabricated using various commercial metal species (Pt, Ru, Pd, Ni, Fe and Co) on carbon. High-angle annular dark-field scanning transmission electron microscopy (HAADF-STEM) analyses indicate that the uniformly distributed Pt, Ru and Pd nanoparticles have average sizes of 2.1, 2.8 and 3.7 nm, respectively, while Ni, Fe and Co metals exist as aggregated forms with sizes of $>6$ nm (Fig. S2, ESI†).

$$NH_3 \rightarrow NH_2^* + H^* \qquad (6)$$

$$N^* + N^* \rightarrow N_2 + 2^* \qquad (7)$$

The catalytic activities of the prepared electrodes are then determined based on overpotentials ($\eta$) and Tafel slopes obtained from linear sweep voltammograms (LSVs). The electrolysis conditions of 6.2 bar and 10 °C are selected to maintain the liquid state of $NH_3$ during the reaction. For the NER, among the screened metals, the Ru electrode exhibits the highest activity with the lowest overpotential ($\eta = 489$ mV at 10 mA cm$^{-2}$, 829 mV at 50 mA cm$^{-2}$, 1113 mV at 100 mA cm$^{-2}$, with $iR$-compensation) (Fig. 2A and Fig. S3A, ESI†). The overpotential at 10 mA cm$^{-2}$ in $NH_3(l)$ electrolysis is higher compared to that observed in water electrolysis using Ru/C ($<400$ mV at 10 mA cm$^{-2}$).[26,27] In addition, the high Tafel slope of Ru/C (381 mV dec$^{-1}$, Fig. S3B, ESI†) further indicates the sluggish kinetics of the NER. Note that the Ru catalyst in the NER electrode undergoes gradual deactivation over time due to nitriding and metal dissolution (Fig. S4 and Table S1, ESI†), consistent with a previous report.[28] Nonetheless, the relatively high activity of Ru/C could likely be associated with the capability of Ru metal to promote both N–H bond scission (eqn (6)) and associative $N_2$ desorption (eqn (7)), as proposed by previous reports.[29,30] Consistently, Hansgen et al. reported that Ru metals facilitate the reaction steps of N–H scission and associative $N_2$ desorption, which are the rate-determining steps of $NH_3$ decomposition.[31]

Then, we further screen potential HER electrocatalysts, demonstrating that the activities toward $H_2$ evolution increase in the following order: Pt/C > Ru/C > Pd/C > Fe/C > Ni/C > Co/C. However the overpotential of Pt/C for the HER is significantly larger (479 mV at 50 mA cm$^{-2}$) than its theoretical potential ($-0.018$ V, Fig. 2B and Fig. S5A, ESI†). Given the low overpotential ($<100$ mV) typically observed in $H_2O(l)$ electrolysis with a Pt/C cathode,[19] the high overpotential in $NH_3(l)$ electrolysis is attributed to the limited $H^+$ dissociation from $NH_4^+$ ($NH_4^+ \rightarrow NH_3 + H^+$) on the Pt surface. The released proton adatoms quickly generate $H_2$, as evidenced by the low Tafel
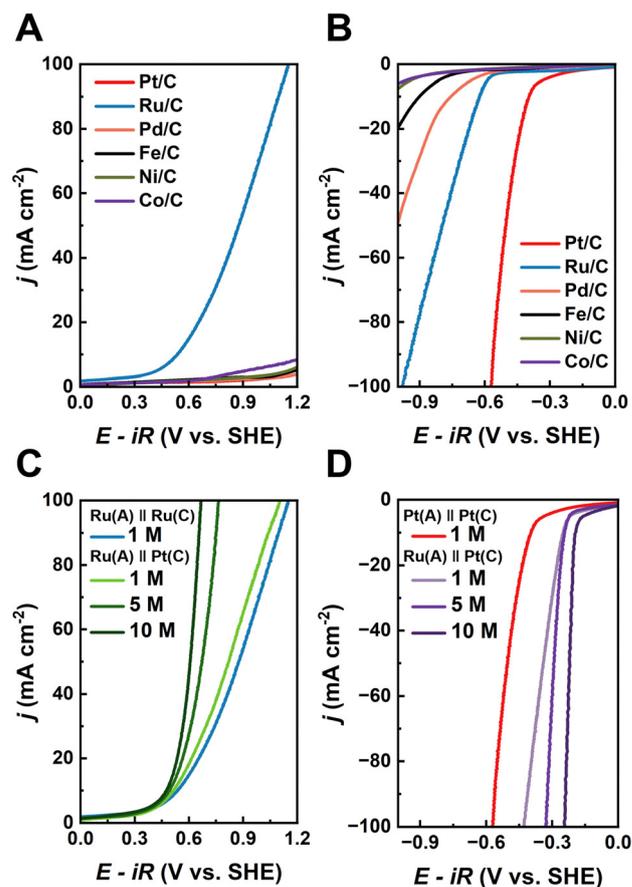


**Fig. 2** Electrochemical characteristics of the as-prepared catalysts determined by linear sweep voltammetry (LSV) with a scan rate of 5 mV s$^{-1}$ under liquid anhydrous $NH_3$ ($NH_3(l)$) conditions at 10 °C and 6.2 bar. (A) and (B) LSVs of the nitrogen evolution reaction (NER) and hydrogen evolution reaction (HER), respectively, using an electrode configuration with identical metals (M‖M, 2.5 μmol cm$^{-2}$) at both the anode and cathode in 1 M $NH_4Br/NH_3(l)$ (see also Fig. S3 and S5, ESI†). (C) LSVs of the NER over Ru‖Ru in 1 M $NH_4Br$ and Ru‖Pt configurations in 1 M, 5 M and 10 M $NH_4Br$ (see also Fig. S6, ESI†). (D) LSVs of the HER over Pt‖Pt in 1 M $NH_4Br$ and Ru‖Pt configurations in 1 M, 5 M and 10 M $NH_4Br$ (see also Fig. S7, ESI†).

slope (121 mV dec$^{-1}$, Fig. S5B, ESI†). Thus, incorporating metals (Ni, Co or Mo, etc.), known to promote $H^+$ dissociation from $NH_4^+$, into Pt metals could potentially reduce the HER overpotential.[31] Based on the screened results, we perform additional electrochemical characterizations using a Ru (anode)‖Pt (cathode) configuration with a 1 M $NH_4Br$ electrolyte. Compared with the Ru‖Ru configuration, the NER overpotential shifts to 775 mV at 50 mA cm$^{-2}$ (Fig. 2C and Fig. S6, ESI†). Likewise, the HER overpotential decreases to its theoretical value compared with that of the Pt‖Pt configuration (Fig. 2D and Fig. S7, ESI†). The results are likely attributed to improved electrochemical properties of each component arising from a decrease in solution resistance ($R_s$) (Fig. S8, ESI†). To promote catalytic activity in the Ru‖Pt configuration, additional $NH_3(l)$ electrolysis is performed by increasing the concentration of the supporting electrolyte from 1 to 5 and 10 M. The electrochemical properties of the anode are slightly improved, reducing the
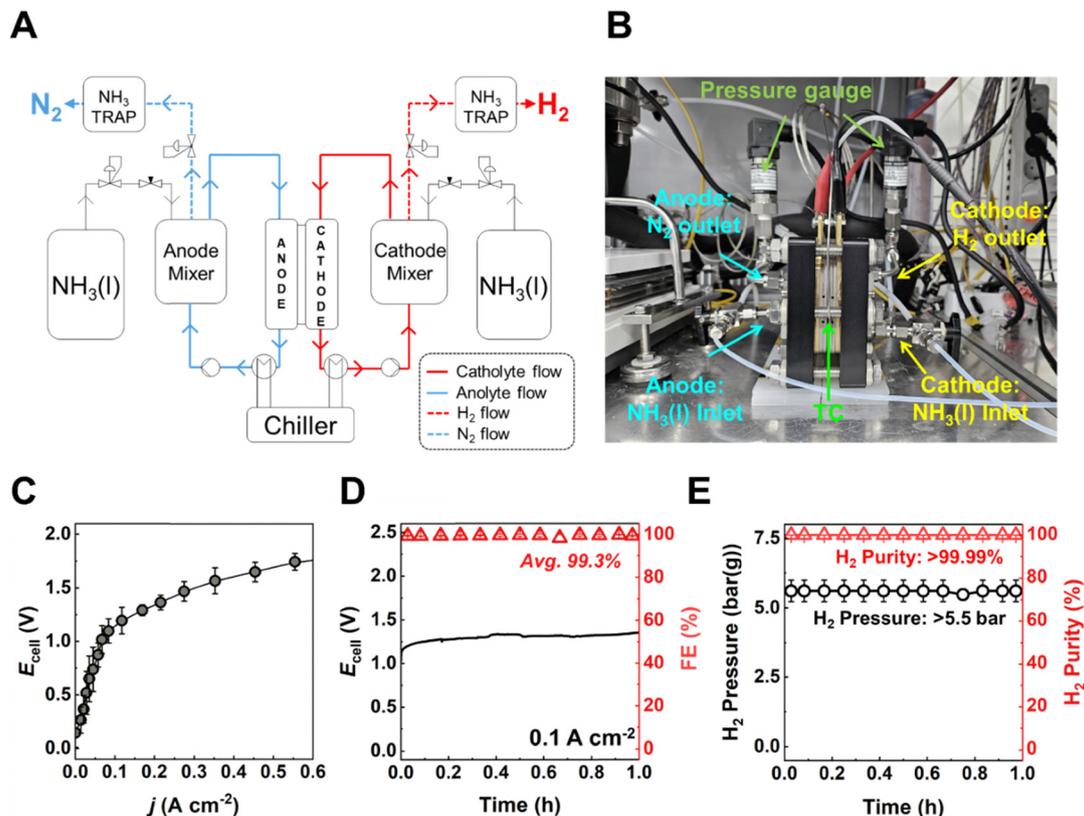
Fig. 3 Continuous production of high-purity, pressurized H₂ using the as-designed NH₃(l) electrolyzer. (A) Process flow diagram (PFD) of the as-designed NH₃(l) electrolysis system. (B) Digital photograph of the NH₃(l) electrolyzer (see also Fig. S10, ESI†). (C) I–V polarization characteristics of the NH₃(l) electrolyzer (anode: 2.5 μmol cm⁻² of Ru/C, cathode: 2.5 μmol cm⁻² of Pt/C) are determined with a scan rate of 5 mA s⁻¹ at a flow rate of 30 mL min⁻¹ and 10 °C, 6.2 bar conditions with 5 M NH₄Br. (D) Potential response of chronopotentiometry measured at 0.1 A cm⁻² and Faradaic efficiency for H₂ production during electrolysis. (E) Purity and pressure of H₂ produced (see also Fig. S11, ESI†).

overpotential ($\eta$) at 50 mA cm⁻² from 775 mV at 1 M to 625 mV at 5 M and 561 mV at 10 M (Fig. S6A, ESI†). In addition, the rate of the NER is further improved, as evidenced by a lower Tafel slope (237 mV dec⁻¹ at 10 M) (Fig. 2C and Fig. S6B, ESI†). The enhanced activity is also associated with the lowering of the charge transfer resistance ($R_{ct}$) as shown by the Nyquist plot obtained from electrochemical impedance spectroscopy (EIS) (Fig. S8A, ESI†): 5.1 Ω at 1 M, 2.5 Ω at 5 M and 2.1 Ω at 10 M. To determine whether the bromide anion (Br⁻) from the supporting electrolyte participated in the NH₃(l) electrolysis, we conducted an additional experiment using NH₄PF₆ as the supporting electrolyte, in which PF₆⁻ functions as an electrochemically inert anion. The resulting LSV profiles using NH₄PF₆ showed negligible differences compared to those obtained with NH₄Br (Fig. S9, ESI†). These results strongly suggest that the Br⁻ was inactive in the anodic process and did not contribute to the formation of byproducts such as Br₂ (2Br⁻ → Br₂ + 2e⁻). Conversely, Pt/C at the cathode exhibits a gentler Tafel slope (40 mV dec⁻¹ at 10 M vs. 90 mV dec⁻¹ at 1 M) with an overpotential of 202 mV at 50 mA cm⁻² in 10 M of electrolyte (Fig. 2D and Fig. S7, ESI†). These results indicate that the enhanced charge and mass transfers under the high concentration of NH₄Br only slightly influence H⁺ dissociation from NH₄⁺, which could likely be the rate-determining step in the HER. Unlike the HER catalyst used in

H₂O(l) electrolysis, developing alternative cathode materials for the HER in NH₃(l) electrolysis is necessary.

To evaluate the practical feasibility of the NH₃(l) electrolysis concept for extracting high-purity H₂, a continuous H₂ production system with a 25 cm² zero-gap type electrolysis cell is constructed (Fig. 3A, B and Fig. S10, ESI†). The NH₃(l) electrolyzer comprises Ru/C as the anode and Pt/C as the cathode, with a cationic exchange membrane. In the continuous electrochemical cell, NH₃(l) is mixed with the NH₄Br electrolyte, and the resulting 5 M NH₄Br/NH₃(l) solution is supplied to both the anode and cathode at 10 °C and 6.2 bar. During the reaction, unreacted NH₃(l) is recirculated into the mixer, and the produced H₂ and N₂ gases, along with less than 1% residual NH₃(g), are purified through an NH₃(g) trap (Fig. 3A). The I–V characteristic of the NH₃(l) electrolysis system shows a cell potential ($E_{cell}$) of ca. 1.1 V at 0.1 A cm⁻² and ca. 1.6 V at 0.5 A cm⁻² (Fig. 3C). This suggests that H₂ production is achievable at a lower potential than the cell potential of ca. 1.4 V at 0.1 A cm⁻² for H₂O(l) electrolysis.[32,33] Despite this advantage, the NH₃(l) electrolysis system still exhibits a much higher cell potential than its theoretical value (0.068 V). Based on the results from both batch and flow electrolysis (Fig. 2 and 3, respectively), the high cell voltage is primarily attributed to activation polarization, while ohmic polarization and concentration overpotential are
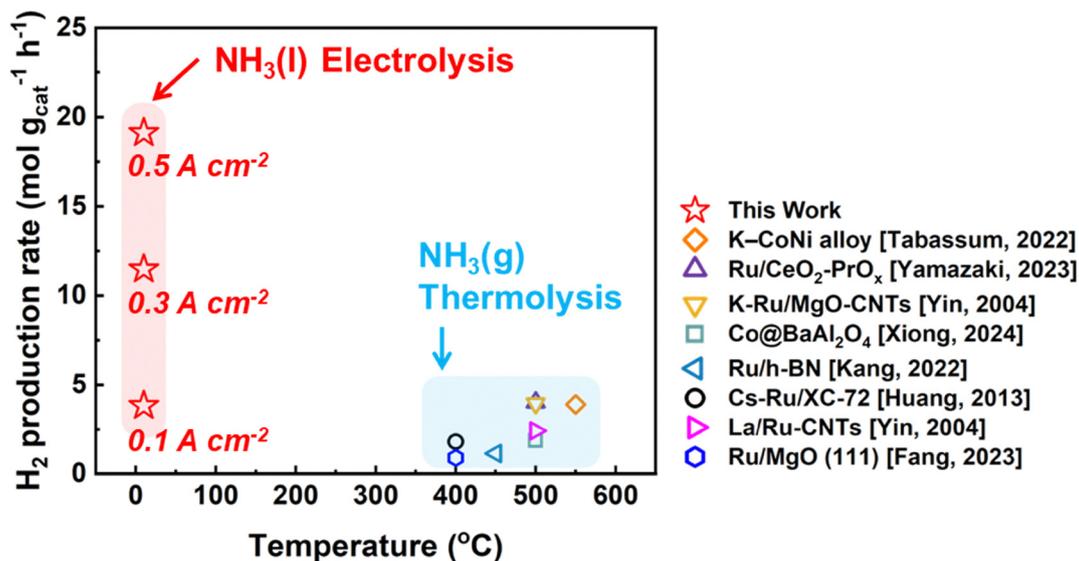
**Fig. 4** Comparison of $H_2$ production rate (mol $g_{cat}^{-1}$ $h^{-1}$) obtained by $NH_3(l)$ electrolysis and $NH_3(g)$ thermolysis. The unit mass of a catalyst for $NH_3(l)$ electrolysis is defined as the mass of the catalyst of the cathode (12.2 mg of Pt/C).

considered negligible. To further determine the efficiency of $H_2$ production, $NH_3(l)$ electrolysis is conducted at a constant current density of 0.1 A $cm^{-2}$ for 1 h. The cell voltage remains below 1.3 V while maintaining a high Faradaic efficiency (FE) of 99.3% (Fig. 3D and Note S4, ESI†). Since only $N_2$ is detected at the anode and only $H_2$ at the cathode, it confirms the complete separation of hydrogen from $N_2$ and $NH_3$, with the $H_2$ purity exceeding 99.99% (Fig. 3E and Fig. S11, ESI†). The high-purity, pressurized $H_2$ ($>$5.5 bar) can be directly connected to a fuel cell without the need for additional pressure-boosting facilities.[34] Compared to previously reported batch type systems, the present $NH_3(l)$ electrolysis system, designed in a zero-gap configuration, enables continuous production of high purity $H_2$ and demonstrates significantly enhanced activity for $H_2$ generation (Table S2, ESI†).

Finally, the rates of $H_2$ production *via* $NH_3(l)$ electrolysis as a function of current density ($j$) are compared with those of reported thermal $NH_3(g)$ decomposition systems (Fig. 4).[6,35–41] The as-designed $NH_3(l)$ electrolysis system produces high-purity and pressurized $H_2$ continuously at 10 °C at a rate of 3.8 mol-$H_2$ $g_{cat}^{-1}$ $h^{-1}$ with a current density ($j$) of 0.1 A $cm^{-2}$, which is comparable to that of state-of-the-art $NH_3(g)$ thermolysis (4.0 mol-$H_2$ $g_{cat}^{-1}$ $h^{-1}$) at 500 °C and 1 bar.[35] When the operating current density is increased to 0.5 A $cm^{-2}$, an FE of 98.8% is achieved and the rate of $H_2$ release further increases to 18.8 mol-$H_2$ $g_{cat}^{-1}$ $h^{-1}$, which is 4.7-fold higher than that of the aforementioned $NH_3(g)$ thermolysis (4.0 mol-$H_2$ $g_{cat}^{-1}$ $h^{-1}$).[35] Additionally, $>$98% of the initial $NH_4Br$ electrolyte is recovered after two cycles (195.9 g → 192.0 g) and reused with negligible activity loss (Fig. S12, ESI†).

## Conclusion

In this proof-of-concept study, to the best of our knowledge, we first demonstrate continuous $H_2$ production *via* direct electrolysis

of anhydrous $NH_3(l)$ at 10 °C under 6.2 bar without a high-cost separation process. Potential catalysts for $NH_3(l)$ electrolysis are initially screened, with Ru/C (anode) and Pt/C (cathode) showing better activities than other metal catalysts. Based on the results, a continuous $NH_3(l)$ electrolysis system equipped with a 25 $cm^2$ zero-gap cell and a cationic exchange membrane is designed. This system demonstrates high-purity and pressurized, continuous $H_2$ production at a rate of 18.8 mol-$H_2$ $g_{cat}^{-1}$ $h^{-1}$, achieving an FE of $>$98.8% at 0.5 A $cm^{-2}$. This electrochemical cell has the potential to replace the thermochemical $NH_3(g)$ decomposition systems currently under development, which require multiple separation processes (*e.g.,* temperature swing adsorption, pressure swing adsorption) and pressurizing components; moreover, the developed system holds significant promises for various commercial applications, particularly as an initial solution for small-scale and decentralized $H_2$ production facilities utilizing $NH_3$ (Table S3, ESI†). Despite these advantages, the obtained cell potential is higher than the theoretical value of 0.068 V. To lower the cell voltage, reducing the cathodic overpotential, enhancing the anodic $N_2$ evolution rate, stability of the electrocatalysts, developing cationic and/or anionic membranes for $NH_3(l)$ electrolysis and improving system durability are essential.

## Experimental section

### Materials

Commercial active metal species (20% Pt, Ru, Pd, Fe, Co and Ni on Vulcan XC-72 conductive carbon black) were purchased from Premetek (Cherry Hill, NJ, US). Nafion solution (5 wt%, DS520) was obtained from Dupont (Wilmington, Delaware, US). Carbon paper (GDS210) for the batch experiment and carbon foam with a gas diffusion layer (EQ-bcgdl-1400S-LD) for the cell test were purchased from CeTech (Taichung, Taiwan) and MTI Korea (Seoul, South Korea), respectively. The cation exchange

membrane was purchased from Solvay (Aquivion E98-09S Brussels, Belgium), and its properties are listed as follows: thickness, 90 μm; tensile stress (MD: Break), 40 MPa; tensile stress (TD: Break), 30 MPa. Isopropanol (anhydrous, 99.5%) and $NH_4Br$ (ACS reagent, ≥99.0%) were purchased from Sigma-Aldrich (St. Louis, MO, US) and used without further purification. Deionized water (DI·$H_2O$) was purified to a resistance of over 18 MΩ cm$^{-1}$ using a water purification system (Pure ROUP 30, Purewater, Gyeong-gi, South Korea). $NH_3(l)$ was supplied from a siphon tank at a purity of >99.99% (free of water and solvent).

### Electrode fabrication

To screen the activities of different metals for the NER and HER, the commercial metals (M = Pt, Ru, Pd, Fe, Co and Ni) on carbon (C, Vulcan XC-72) are loaded on the carbon paper by the slurry coating method. **In a typical batch experiment**, an active metal amount is set to 2.5 μmol cm$^{-2}$. First, a metal precursor is initially dissolved in 530 μL of the mixture of isopropanol (IPA) and DI $H_2O$ (1:1, vol%), and 100 μL of Nafion solution is added to the IPA/$H_2O$ solution as a binder, making a total 630 μL. This precursor solution is then sonicated for 1 h to produce a well-dispersed solution, referred to as an 'ink'. Next, 31.5 μL of the ink is dropped onto 1 cm$^2$ of carbon paper to fabricate the electrode for screening the activities. Then, the prepared electrodes are dried in a vacuum for 30 min at 25 °C. **For full-cell operation**, the metal loadings for the NER and HER electrodes are also maintained at 2.5 μmol cm$^{-2}$ (the total weight of Ru/C, 6.3 mg) for the anode and 2.5 μmol cm$^{-2}$ (the total weight of Pt/C, 12.2 mg) for the cathode, respectively. The ink solution containing the mixture of IPA and DI $H_2O$ (1:1, vol%, 2.12 mL) and 5 wt% Nafion solution (400 μL) is prepared. Next, 78.8 μL of the ink is dropped onto 25 cm$^2$ of carbon foam and then dried in a vacuum for 30 min at 25 °C.

### Electrochemical measurements in the batch reactor

Electrochemical analyses for active metal screening are conducted using a high-pressure three-electrode batch reactor at 10 °C and 6.2 bar (specific cell configuration in Fig. S1, ESI†) with the addition of the supporting electrolyte ($NH_4Br$, 0–10 M). The Ag/AgCl (3.4 M KCl, Innovative Instruments, Inc., Tampa, FL, US) reference electrode, covered with polyetheretherketone (PEEK), along with the working and counter electrodes, is connected to a potentiostat (VSP with 4A booster; Bio-Logic Science Instruments, Seyssinet-Pariset, France) for electrochemical measurements. Prior to an experiment, the reactor is purged with Ar for 1 h to remove residual air. $NH_3(l)$ is then supplied from a siphon-type container to the reactor, and a liquid regulator is used to maintain the reaction pressure at 6.2 bar. The applied potential is recalculated based on experimental conditions, with further details provided in Notes S1–S3 (ESI†). Analyses with linear sweep voltammetry (LSV) are performed at a scan rate of 5 mV s$^{-1}$, with the scan direction selected properly for each half-reaction: an oxidative sweep for the anodic reaction (NER) and a reductive sweep for the cathodic reaction (HER). Before conducting an experiment,

85% $iR$ compensation was applied using the value of solution resistance ($R_s$) estimated from electrochemical impedance spectroscopy (EIS). To ensure an improved evaluation of intrinsic kinetics, the remaining 15% of uncompensated resistance was additionally corrected. The Nyquist plot from the EIS is obtained from 100 kHz to 100 MHz at +1.0 $V_{SHE}$ for the anode and −1.2 $V_{SHE}$ for the cathode. Tafel plots are calculated along the linear portion of the LSV.

### Electrochemical measurements in the full-cell

Before an experiment, the $NH_3(l)$ electrolyzer is purged with Ar for 1 h to remove residual air. In a typical electrolysis experiment, $NH_3(l)$ and the supporting electrolyte (5 M $NH_4Br$) are initially homogenized using a magnetic stirrer in the anode and cathode mixers (200 mL) (refer to Fig. 3A). The resulting solutions are then supplied into the anode and cathode at a flow rate of 30 mL min$^{-1}$, followed by continuous circulation for 3 h to stabilize the cell. This procedure allows both the anode, cathode and membrane to be fully wet by $NH_3(l)$. Note that the Aquivion membrane, which features perfluorosulfonic acid (PFSA) functionality, is reported to exhibit $NH_4^+$ conductivity of *ca.* 30 mS cm$^{-1}$,[42] making it suitable for the purpose of this study.[43–47] The 25 cm$^2$ zero-gap type electrolyzer is operated at 10 °C and 6.2 bar using a DC power supply XG 20-76 (20 V, 76 A, Ametek, Berwyn, PA, US) with the current sweep (scan rate: 5 mA s$^{-1}$) and constant current methods. After the $NH_3(l)$ splitting reaction, unreacted $NH_3(l)$ is pumped back to each mixer for reuse. Finally, the obtained $H_2$ and $N_2$ gases are analyzed using a mass flow meter (F-201C; Bronkhorst, Ruurlo, Netherlands) and gas chromatography (YL6500; Young-In Chromass, Gyeong-gi, South Korea). Specific cell configuration and process flow diagrams are shown in Fig. 3A and Fig. S10 (ESI†).

## Author contributions

Conceptualization, S. H., C. H. L. and C. W. Y.; methodology, S. H., J. S. H., H. L., C. H. L. and C. W. Y.; investigation, S. H. and H. L.; writing – original draft, S. H. and C. W. Y.; validation, J. S. H., J. S. L., C. H. L. and K. C. and C. W. Y.; writing – review and editing, S. H., J. S. H., J. S. L., H. L., C. H. L., K. C. and C. W. Y.; project administration, C. H. L., K. C. and C. W. Y.; funding acquisition, C. W. Y.; supervision, C. W. Y.

## Data availability

The data supporting this article have been included as part of the ESI.†

## Conflicts of interest

The authors declare no competing financial interest.

## Acknowledgements

# References

1 L. Schlapbach and A. Züttel, *Nature*, 2001, **414**, 353–358.

2 F. Chang, W. Gao, J. Guo and P. Chen, *Adv. Mater.*, 2021, **33**, 2005721.

3 U. B. Demirci and P. Miele, *Energy Environ. Sci.*, 2011, **4**, 3334–3341.

4 E. Spatolisano, L. A. Pellegrini, A. R. de Angelis, S. Cattaneo and E. Roccaro, *Ind. Eng. Chem. Res.*, 2023, **62**, 10813–10827.

5 F. Restelli, E. Spatolisano, L. A. Pellegrini, A. R. De Angelis, S. Cattaneo and E. Roccaro, *Int. J. Hydrogen Energy*, 2024, **52**, 532–547.

6 S. Kang, J. Cha, Y. S. Jo, Y. J. Lee, H. Sohn, Y. Kim, C. K. Song, Y. Kim, D. H. Lim, J. Park and C. W. Yoon, *Adv. Mater.*, 2023, **35**, 2203364.

7 D. R. MacFarlane, P. V. Cherepanov, J. Choi, B. H. Suryanto, R. Y. Hodgetts, J. M. Bakker, F. M. F. Vallana and A. N. Simonov, *Joule*, 2020, **4**, 1186–1205.

8 S. Sayas, N. Morlanés, S. P. Katikaneni, A. Harale, B. Solami and J. Gascon, *Catal. Sci. Technol.*, 2020, **10**, 5027–5035.

9 S. Chatterjee, R. K. Parsapur and K.-W. Huang, *ACS Energy Lett.*, 2021, **6**, 4390–4394.

10 D. Tang, G.-L. Tan, G.-W. Li, J.-G. Liang, S. M. Ahmad, A. Bahadur, M. Humayun, H. Ullah, A. Khan and M. Bououdina, *J. Energy Storage*, 2023, **64**, 107196.

11 Y. Yang, J. Kim, H. Jo, A. Seong, M. Lee, H.-K. Min, M.-G. Seo, Y. Choi and G. Kim, *J. Mater. Chem. A*, 2021, **9**, 11571–11579.

12 M. Cooper and G. G. Botte, *J. Electrochem. Soc.*, 2006, **153**, A1894.

13 J. Gwak, M. Choun and J. Lee, *ChemSusChem*, 2016, **9**, 403–408.

14 N. Akagi, K. Hori, H. Sugime, S. Noda and N. Hanada, *J. Catal.*, 2022, **406**, 222–230.

15 D. J. Little, M. R. Smith III and T. W. Hamann, *Energy Environ. Sci.*, 2015, **8**, 2775–2781.

16 N. Hanada, S. Hino, T. Ichikawa, H. Suzuki, K. Takai and Y. Kojima, *Chem. Commun.*, 2010, **46**, 7775–7777.

17 B.-X. Dong, T. Ichikawa, N. Hanada, S. Hino and Y. Kojima, *J. Alloys Compd.*, 2011, **509**, S891–S894.

18 A. J. Shih, M. C. Monteiro, F. Dattila, D. Pavesi, M. Philips, A. H. da Silva, R. E. Vos, K. Ojha, S. Park and O. van der Heijden, *Nat. Rev. Methods Primers*, 2022, **2**, 84.

19 M. Chatenet, B. G. Pollet, D. R. Dekel, F. Dionigi, J. Deseure, P. Millet, R. D. Braatz, M. Z. Bazant, M. Eikerling, I. Staffell, P. Balcombe, Y. Shao-Horn and H. Schäfer, *Chem. Soc. Rev.*, 2022, **51**, 4583–4762.

20 K. Siddharth, Y. Chan, L. Wang and M. Shao, *Curr. Opin. Electrochem.*, 2018, **9**, 151–157.

21 C. Zhong, W. Hu and Y. Cheng, *J. Mater. Chem. A*, 2013, **1**, 3216–3238.

22 X. Ding, Y. Ji, H. Huang, J. Huang, S. Chen, C. Yang, F. Li and M. Luo, *Chem. Catal.*, 2024, **4**, 100932.

23 A. Allagui, M. Oudah, X. Tuaev, S. Ntais, F. Almomani and E. A. Baranova, *Int. J. Hydrogen Energy*, 2013, **38**, 2455–2463.

24 N. S. Hassan, A. A. Jalil, R. Saravanan, N. M. Izzuddin, M. B. Bahari, D. Prasetyoko and R. E. Nugraha, *J. Mater. Chem. A*, 2024, **12**, 23202–23217.

25 L. Carmichael and B. Sage, *Ind. Eng. Chem. Res.*, 1952, **44**, 2728–2732.

26 D. Kong, C. Meng, Y. Wang, X. Chen, J. Zhang, L. Zhao, J. Ji, L. Zhang and Y. Zhou, *Appl. Catal., B*, 2024, **343**, 123578.

27 Y. Gorlin and T. F. Jaramillo, *J. Am. Chem. Soc.*, 2010, **132**, 13612–13614.

28 D. J. Little, D. O. Edwards, M. R. Smith III and T. W. Hamann, *ACS Appl. Mater. Interfaces*, 2017, **9**, 16228–16235.

29 F. García-García, A. Guerrero-Ruiz and I. Rodríguez-Ramos, *Top. Catal.*, 2009, **52**, 758–764.

30 J. C. Ganley, F. Thomas, E. Seebauer and R. I. Masel, *Catal. Lett.*, 2004, **96**, 117–122.

31 D. A. Hansgen, D. G. Vlachos and J. G. Chen, *Nat. Chem.*, 2010, **2**, 484–489.

32 L. Tao, F. Lv, D. Wang, H. Luo, F. Lin, H. Gong, H. Mi, S. Wang, Q. Zhang and L. Gu, *Joule*, 2024, **8**, 450–460.

33 Y. Hong, S. C. Cho, S. Kim, H. Jin, J. H. Seol, T. K. Lee, J.-K. Ryu, G. M. Tomboc, T. Kim and H. Baik, *Adv. Energy Mater.*, 2024, **14**, 2304269.

34 J. Hoeflinger and P. Hofmann, *Int. J. Hydrogen Energy*, 2020, **45**, 29246–29258.

35 K. Yamazaki, M. Matsumoto, M. Ishikawa and A. Sato, *Appl. Catal., B*, 2023, **325**, 122352.

36 S. Yin, B. Xu, S. Wang, C. Ng and C. Au, *Catal. Lett.*, 2004, **96**, 113–116.

37 D.-C. Huang, C.-H. Jiang, F.-J. Liu, Y.-C. Cheng, Y.-C. Chen and K.-L. Hsueh, *Int. J. Hydrogen Energy*, 2013, **38**, 3233–3240.

38 S.-F. Yin, B.-Q. Xu, C.-F. Ng and C.-T. Au, *Appl. Catal., B*, 2004, **48**, 237–241.

39 P. Xiong, Z. Xu, T.-S. Wu, T. Yang, Q. Lei, J. Li, G. Li, M. Yang, Y.-L. Soo, R. D. Bennett, S. P. Lau, S. C. E. Tsang, Y. Zhu and M. M.-J. Li, *Nat. Commun.*, 2024, **15**, 420.

40 H. Fang, S. Wu, T. Ayvali, J. Zheng, J. Fellowes, P.-L. Ho, K. C. Leung, A. Large, G. Held, R. Kato, K. Suenaga, Y. I. A. Reyes, H. V. Thang, H.-Y. T. Chen and S. C. E. Tsang, *Nat. Commun.*, 2023, **14**, 647.

41 H. Tabassum, S. Mukherjee, J. Chen, D. Holiharimanana, S. Karakalos, X. Yang, S. Hwang, T. Zhang, B. Lu, M. Chen, Z. Tang, E. A. Kyriakidou, Q. Ge and G. Wu, *Energy Environ. Sci.*, 2022, **15**, 4190–4200.

42 J. Peng, K. Lou, G. Goenaga and T. Zawodzinski, *ACS Appl. Mater. Interfaces*, 2018, **10**, 38418–38430.

43 L. Xu, D. Liu, W. Liu, J. Yang, J. Huang, X. Wang and Q. He, *ACS Omega*, 2022, **7**, 20634–20643.

44 R. Lan and S. Tao, *ECS Electrochem. Lett.*, 2013, **2**, F37.

45 V. Signorini, A. Askin, C. Oldani, M. Minelli and M. Giacinti Baschetti, *J. Membr. Sci.*, 2024, **697**, 122564.

46 Y. He and E. L. Cussler, *J. Membr. Sci.*, 1992, **68**, 43–52.

47 K. Wakimoto, W.-W. Yan, N. Moriyama, H. Nagasawa, M. Kanezashi and T. Tsuru, *J. Membr. Sci.*, 2022, **658**, 120718.